



Single-step sintering of zirconia ceramics using hydroxide precursors and Spark Plasma Sintering below 400 °C

C. Elissalde^{a,*}, U-C. Chung^a, M. Josse^a, G. Goglio^a, M.R. Suchomel^a, J. Majimel^a, A. Weibel^b, F. Soubie^a, A. Flaureau^b, A. Fregeac^b, C. Estournès^b

^a CNRS, Univ. Bordeaux, ICMCB, UMR 5026, 87 avenue du Dr A. Schweitzer, 33608 Pessac, France

^b CIRIMAT, Université de Toulouse, CNRS, Université Toulouse 3 - Paul Sabatier, 118 route de Narbonne 31062 Toulouse cedex 9, France

ARTICLE INFO

Article history:

Received 3 April 2019

Accepted 30 April 2019

Available online 9 May 2019

Keywords:

Spark Plasma Sintering

Amorphous oxides precursors

Nanostructured zirconia ceramics

Polymorphic phase transformation

Hardness

ABSTRACT

The densification of zirconia at very low temperatures (<400 °C) requires enhanced synergy between thermodynamics and kinetics. This work demonstrates an efficient single step approach combining amorphous hydrated zirconia and Spark Plasma Sintering at 350 °C and 600 MPa. The resulting zirconia ceramics exhibit a cohesive nanostructure with small average grain sizes (20 nm) and a predominantly monoclinic structural polymorph confirmed by both X-ray scattering analyses and High Resolution Transmission Electronic Microscopy. Remarkable Vickers hardness of 3.8 GPa for high level of porosity (30%) is explained by the density and homogeneous distribution of grains boundaries and meso/microporosities.

© 2019 Acta Materialia Inc. Published by Elsevier Ltd. All rights reserved.

The development of more energy and environmentally friendly manufacturing processes has recently encouraged intensive research on low-temperature sintering [1]. This work has opened new opportunities in topics such as the integration of inorganic materials with varying structures, processing of new composites, nanostructured ceramics and the co-sintering of ceramics, polymers or metals [2–4]. Emergent processes allowing the reduction of sintering temperatures have also led to the development of new materials and composites for microwave devices (Ultra Low Temperature Co-fired Ceramics) [5]. In addition to the sintering techniques categorized as Field Assisted Sintering Technology (e.g. Flash Sintering, Spark Plasma Sintering (SPS)) that are well recognized for advantageous enhanced kinetics [6–8], the exploration of non-equilibrium sintering, through transient liquid phase or by using solvent assisted sintering (Cold Sintering Process, Hydro-Solvothermal Sintering) was also shown to be particularly efficient for very low temperature sintering of functional oxides such as ZnO, BaTiO₃, α-Quartz and composites [9–15]. Cool-SPS has also demonstrated the solvent-free sintering of thermodynamically fragile materials, including reactive sintering of hydrated precursors at temperatures below 400 °C [16–18]. Although these new methods have been applied to an impressive number and variety of compounds, the promise of low temperature sintering processes still remains limited for the sintering of refractory oxides such as zirconia [19]. The structural versatility of zirconia and its link with functional properties has given rise to increasing interest from both a scientific and applications point of view. Since the discovery of its

reinforcement by phase transformation, zirconia (ZrO₂) has become a reference in the field of ceramics [20]. From thermal barriers to biomaterials, zirconia is used in multiple applications [21,22]. High tensile strength and tenacity were observed in two-phase samples with tetragonal and monoclinic as the major and minor phases, respectively [23]. Doping zirconia with oxides is necessary in order to stabilize the tetragonal phase at room temperature, for example Yttria (Y₂O₃) is one of the most commonly used dopants (e.g. 3 mol% (3Y-TZP)). However conventional sintering requires temperatures as high as 1500 °C and can result in the stabilization of the additional cubic phase that has a detrimental impact on aging resistance. The attractive features of zirconia are thus closely linked to the control of crystalline phases and depend on defect chemistry for charge compensation associated with aliovalent substitutions. In addition, a retention of nanostructure in the final ceramic is expected to improve properties. The metastable phase diagram, and the control of both grain size and of defect chemistry in the processing of zirconia ceramics are thus distinct issues that must be mastered, all of which strongly depend on the sintering conditions. To meet the challenge of low temperature sintering of zirconia in one step, our approach described in this work targets the enhanced synergy between thermodynamic and kinetics effects by combining Spark Plasma Sintering (SPS) processing with amorphous hydrated zirconium oxide as precursor. As mentioned above, key performance criteria for zirconia ceramics are intimately tied to structural and microstructural features (phase stabilization, grain size, level of porosity) which require tuning for the targeted properties of specific applications (biomedical, fuel cells, thermal barrier, abradable coating). Inspired by the recent advances from Cold Sintering Process, Hydro/Solvothermal sintering, SPS and Cool-

* Corresponding author at: ICMCB-CNRS, 87 Av. Dr. Schweitzer, 33608 Pessac, France.
E-mail address: catherine.elissalde@icmcb.cnrs.fr (C. Elissalde).

SPS, our work here demonstrates that single-step low temperature SPS of amorphous hydrated zirconia is highly relevant to fulfill the challenging requirements for numerous applications.

A commercial $\text{Zr}(\text{OH})_4$ powder (99.9%, 40 nm) was purchased from US Research Nanomaterials, Inc. Houston, TX., USA. Thermogravimetric and Infrared absorption analyses were conducted on the raw powder (Figs. S1, S2). *In situ* variable temperature Powder X-ray Diffraction (PXRD) studies were performed from room temperature up to 500 °C (Fig. S3). The hydroxide precursor was sintered using a Dr Sinter 515S, Syntex, Japan, loading directly the amorphous powder in a 10 mm tungsten carbide mold. A pressure of 600 MPa was applied and the temperature was raised up to 350 °C with a heating rate of 50 °C/min. The pressure was maintained at 350 °C during the temperature dwell of 10 min.

Pair Distribution Function (PDF) analysis was performed on X-ray scattering data collected at ambient temperature on powder samples loaded inside 1.0 mm diameter polyamide capillaries at beamline 11-ID-B of the Advanced Photon Source at Argonne National Laboratory, using 59 keV X-rays ($\lambda \approx 0.211$ Å) and a large-area detector. The software programs pyFAI [24] and PDFgetX3 [25] were used to obtain atomic pair distribution functions $G(r)$ which were subsequently analyzed with structure modeling capabilities in the TOPAS 6.0 software package [26]. Instrumental resolution and damping terms have been determined by fitting data obtained from a standard Ni powder calibration sample. Five samples were measured, the initial $\text{Zr}(\text{OH})_4$ precursor, the ceramic obtained by SPS at 350 °C and three reference samples corresponding to commercial powders, monoclinic ZrO_2 with large micron crystallite size, tetragonal ZrO_2 (3%mol. Yttria) with large crystallite size (>100 nm) and nanocrystallite size (~10 nm). SPS ceramic was analyzed by Raman spectroscopy (confocal microscope RAMAN Labram HR 800 Yvon Jobin, 633 nm) in three different zones. Data collection was performed in the range 100–700 cm^{-1} (240 s of measurement per accumulation and 3 accumulations per segment). Phase percentages were calculated taking into account an average spectrum over the three collected. HRSEM micrographs were obtained using a field emission-gun scanning electron microscopy (FESEM, JEOL JSM 7800F). HRTEM experiments were performed on 110 JEOL 2200 FS equipped with electron field-emission gun operating at 200 kV with a point-to-point resolution of 0.23 nm. High resolution micrographs and videos were acquired with a Gatan Ultrascan CCD 2×2 k camera and digital diffractograms were calculated with the Gatan Digital Micrograph software. Mechanical tests were performed on polished surface samples by loading 2.94 N at room temperature during 10 s with a Vickers indenter (Mitutoyo HM 200).

The diagonals of the indentation were measured using an optical microscope attached to the indenter. The calculated microhardness value corresponds to the average of ten measurements.

Microstrain and defect concentration are high in the amorphous phase, with both dehydration and crystallization involving grain rearrangement which can contribute to densification in the primary stages. In order to determine optimized sintering conditions, the dehydration through TGA and the sequence of structural changes as a function of temperature through *in situ* variable temperature PXRD were first investigated (Figs. S1, S3). Complete dehydration at 200 °C (total mass loss of 42%) is followed at 300 °C by the onset of crystallization of the amorphous phase into tetragonal phase, confirming previous reports of the crystallization of a metastable high temperature phase from an amorphous precursor [27,28]. The lower surface energy of the tetragonal phase compared to the monoclinic phase and higher lattice strain were considered to explain the formation of metastable tetragonal zirconia at low temperature from amorphous precursor [29–31]. However the reported temperature windows for crystallization and the critical size towards phase stabilization do not meet a general agreement and depend on the method of preparation of the initial zirconium hydroxide [32]. In the work reported here, an abrupt increase of the tetragonal (101) peak is observed in the PXRD scans recorded between 350 and 400 °C. The transition towards a monoclinic phase starts above 400 °C leading to the coexistence of the two polymorphs by 500 °C (approximate fractions of 96% tetragonal/4% monoclinic by PXRD analysis). The amount of monoclinic phase was subsequently shown to increase first slightly on re-cooling and then much more abruptly down to 25 °C. On the basis of these TGA and *in situ* PXRD preliminary investigations, the SPS sintering temperature was set at 350 °C under a pressure of 600 MPa (dwell 10 min) to prevent grain growth and to favor densification.

Quantitative phase analysis conducted by Raman spectroscopy revealed that the majority phase in the SPS processed ceramics adopts the monoclinic polymorph symmetry with a percentage reaching 80%. The strong and sharp monoclinic doublet at 180 and 192 cm^{-1} and the tetragonal band at 148 cm^{-1} , respectively indexed m and t in Fig. 1, were considered for phase quantification [33].

PDF and Rietveld X-ray analysis provided greater structure detail, including insight into local ordering of the initial hydroxide precursor. The PDF data of the $\text{Zr}(\text{OH})_4$ powder definitively show that very short range atomic ordering is present within the “amorphous” hydroxide powder (Fig. 2a), and that this local structure can be well approximated by the ZrO_2 monoclinic polymorph ($P2_1/c$) crystallographic model, in

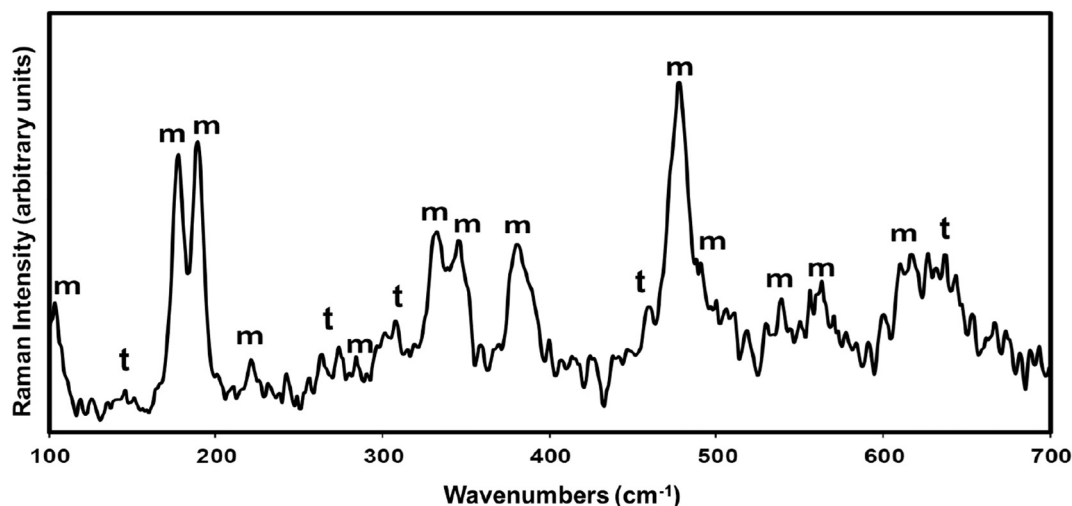


Fig. 1. Raman spectrum of ZrO_2 ceramic obtained by SPS at 350 °C from $\text{Zr}(\text{OH})_4$ precursor (m and t refer to monoclinic and tetragonal phases, respectively).

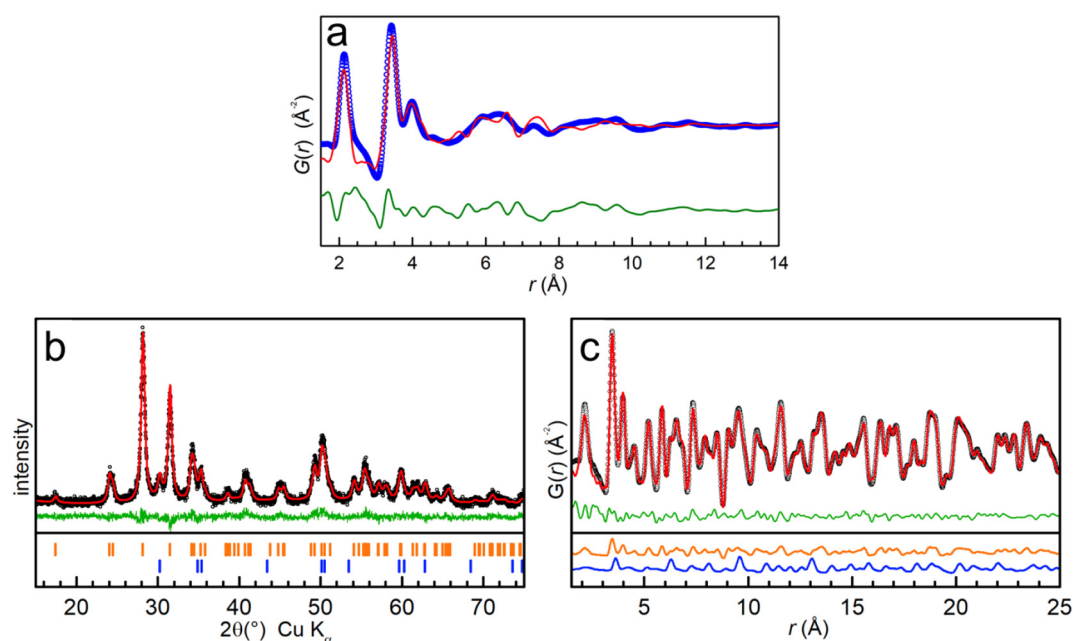


Fig. 2. a–c. a) Fit of $G(r)$ for the $Zr(OH)_4$ reference powder using a monoclinic ZrO_2 structural model with a very small domain particle size <10 Å. ($R_{wp} = 35\%$, refined in space group $P2_1/c$ with $a = 4.942(2)$ Å, $b = 5.321(2)$ Å, $c = 5.178(2)$ Å, and monoclinic angle $\beta = 97.31(5)^\circ$). Experimental data are plotted as blue circles, with the calculated fit and difference curves as red and green lines, respectively. b–c) Plots showing combined refined fit to powder XRD data (b) and PDF $G(r)$ (c) for powder data measured on the SPS ceramic. Experimental data are shown as black circles, with the calculated fit and difference curves as red and green lines, respectively. For reference, for the XRD data (a) the lower panel shows 2θ position tick mark for monoclinic (orange) and tetragonal (blue) phases, while for the PDF data (b) simulated $G(r)$ curves for monoclinic (orange) and tetragonal (blue) phases are plotted with compressed intensity scaling.

agreement with recent literature reports [34,35]. In particular, for low $r < 10$ Å, clear features well matching with expected peaks from first neighbor Zr–O pairs (~ 2.1 Å) and Zr–Zr pairs (~ 3.5 Å) are observed.

It is suspected that the mismatch between the experimental and calculated intensity in the $G(r)$ for $r \approx 2.5$ Å arises from O–O pairs in uncoordinated H_2O or OH^- groups present in the precursor, as discussed for $Zr(OH)_4$ by King et al. [34]. Moreover, PDF studies of liquid H_2O show that the most intense PDF peak lies at (~ 2.5 Å) [36]. However, incorporating these details into the $Zr(OH)_4$ data model was beyond the scope of the current work reported here.

Table 1

Summary of combined PDF $G(r)$ and XRD Rietveld refinements performed with the TOPAS V6 software, using a mixed monoclinic and tetragonal phase model, for powder data of the SPS ceramic. Lattice parameters and atomic positions for both phases were constrained across both datasets during the refinement. Note that listed B_{iso} values are from the XRD dataset fit; in the refined PDF model the B_{iso} values are similar but include an r -dependent broadening term. Crystallite size terms are refined separately for XRD and PDF data, as they are not equivalent size models. The combined fit has a total R_{wp} of 10.8%.

Dataset	XRD	PDF
Measurement	Cu-K α PANalytical X'pert	APS beamline 11-ID-B, 59 keV
Weighting	1	18,000
R_{wp}	8.3%	12.9%
Monoclinic ZrO_2 ($P2_1/c$)	Crystallite size (nm) Phase fraction Lattice values	12 0.95 $a = 5.1534(1)$ Å, $b = 5.2088(1)$ Å, $c = 5.3239(1)$ Å, $\beta = 99.339(2)^\circ$
Site	x y z	B_{iso} (\AA^2) 0.6 1.0 1.0
Tetragonal ZrO_2 ($P4_2/nmc$)	Crystallite size (nm) Phase fraction Lattice values	11 0.05 $a = 3.6382(5)$ Å, $c = 5.075(1)$ Å
Site	x y z	B_{iso} (\AA^2) 0.6 0.21 1.0

Fig. 2b–c illustrates the refined fits to PXRD and PDF data for the SPS ceramic. Preliminary fits using a purely monoclinic $P2_1/c$ model to fit the PDF data from the SPS ceramic showed broad agreement establishing that the SPS ceramic predominantly contains the monoclinic phase.

However, the higher PDF statistical fit ($R_{wp} = 17.3\%$) is worse than that observed in refinements of monoclinic and tetragonal ZrO_2 reference samples ($R_{wp} = 10\%$) (Fig. S4a–c). Adding an additional minority phase of tetragonal $P4_2/nmc$ ZrO_2 polymorph to the PDF refinement of the majority monoclinic SPS ceramic improves the overall fit agreement ($R_{wp} = 12.9\%$) (Fig. 2c). This is in agreement with Rietveld refinements of laboratory PXRD data (Fig. 2b) which also show the presence of peaks from a minority tetragonal polymorph phase (<10 w%). Note that the slight discrepancy with the evaluation of the fraction of monoclinic

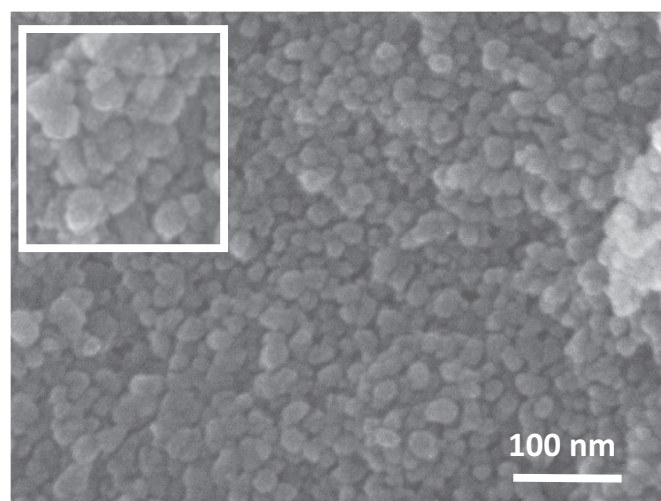


Fig. 3. HRSEM images of the fracture surface of the ZrO_2 ceramics processed by Spark Plasma Sintering at 350°C starting from $Zr(OH)_4$ precursors. Insert: zoom on the formation of grain boundaries.

Table 2

Comparison of Vickers Hardness of zirconia SPS ceramics obtained from different precursors.

Initial powder	Setpoint temperature (°C)	Applied pressure MPa	Dwell time (min)	Porosity (%)	% polymorphs after SPS	Vickers hardness (GPa)	Standard deviation
ZrOH ₄ (US nano)	350	600	10	~20–30	85 (monoclinic) /15 (tetragonal)	3.805	14
6YSZ (Tosoh)	1050	50	1	34	100 (tetragonal)	3.462	11
5.1YSZ (sol gel)	1050	50	1	32.8	100 (tetragonal)	3.187	35

phase by Raman can arise from the different penetration depth probed [37].

The SPS ceramic PDF data show damping of $G(r)$ intensity at high r values beyond that expected from instrumental Q_{damp} term. Therefore, separate ZrO_2 crystallite domain diameters were included in the PDF fits for the monoclinic and tetragonal polymorphs, which refine to ~12 nm and ~11 nm, respectively. These values are in good agreement with crystallite size estimated from Rietveld refinements of laboratory PXRD data of ~15 nm and ~12 nm, respectively. Because the monoclinic phase fraction is much greater than the tetragonal phase, it is likely difficult to extract very accurate domain size values of the tetragonal component. Full details of refined parameters for two phase fits of SPS ceramic are given in Table 1.

Microstructural analysis by HRSEM reveals a homogeneous nanostructure (Fig. 3). Image analysis (Image J- mean linear intercept method and considering about a hundred grains) from naturally fractured surfaces of the SPS ceramic confirms an average grain size of 15 ± 4 nm. The observed microstructure is consistent with 25–30% of porosity (determined by geometric method) but clearly reveals effective consolidation and the formation of grain boundaries (Insert Fig. 3).

The hardness depends significantly on the porosity level but does not seem to be significantly affected by the nature of the crystalline phase [19,38]. The literature reports hardness on the order of 10–13 GPa for zirconia ceramics densified to >95% whether they are pure tetragonal or monoclinic [39,40]. The obtained average hardness value in the case of ZrO_2 sintered at 350 °C by SPS from $ZrOH_4$ reaches 3.8 GPa. This value (see Table 2) is comparable to the ones obtained for yttria stabilized zirconia ceramics starting from ZrO_2 -6Y (commercial powder Tosoh – referred in Table 2 as 6YSZ) and ZrO_2 -5.1Y (sol-gel synthesis - referred in Table 2 as 5.1YSZ) sintered by SPS at 1050 °C with a comparable level of porosity and final grain size in the same range (~50 nm) [41]. Note that the hardness of cold-sintered zirconia

ceramics processed at 180 °C (85% relative density – mixed tetragonal/monoclinic 50/50) is ~0.5 GPa. An annealing at temperature higher than 900 °C is necessary to increase the value up to 4 GPa [19].

Microstructure to hardness relationships have been largely studied in particular for stabilized zirconia ceramics. However a consensus about grain size effect on the yield strength has not been yet found and is not as well understood as in the case of metals and metal alloys (Hall-Petch effect). Considering the very small grain size (15 nm) of the SPS ceramics, the high concentration of grain boundaries would play a predominant role and contribute to the unexpected mechanical properties obtained. HRTEM was used to probe their specificities when using SPS at a sintering temperature as low as 350 °C. It is worth noting that highly crystallized particles are observed in a size range that is in full agreement with the one evaluated from PDF and XRD Rietveld refinements (Table 1). HRTEM observations reveal that most of the particles are monocrystalline and crystallize in the monoclinic system (Fig. 4a). The second noticeable feature is the presence of plastic interfaces (with evaluated lattice misfits ranging from 3 to 35% depending on grain orientations and grain boundary configurations) that are highlighted by the presence of dislocation networks as illustrated on the inset of Fig. 4a. If there is no evidence of the presence of residual amorphous phase that could lead to weaker GB, cavity nucleation occurs at grain boundary triple junction contributing to the significant global mesoporosity. Grain boundary triple junctions are also formed by particles of different sizes (Fig. 4b), in particular several crystallites of diameter lower than 5 nm whose structure does not match with the pure monoclinic structure determined by PDF and XRD refinements but rather with a slightly distorted one. Tetragonal crystallites have not been identified among the observed particles by HRTEM. Their expected size of 12 nm (from PDF and PXRD) is greater than that of the small distorted monoclinic particles described above and thus questions on the stabilization of the tetragonal phase through a

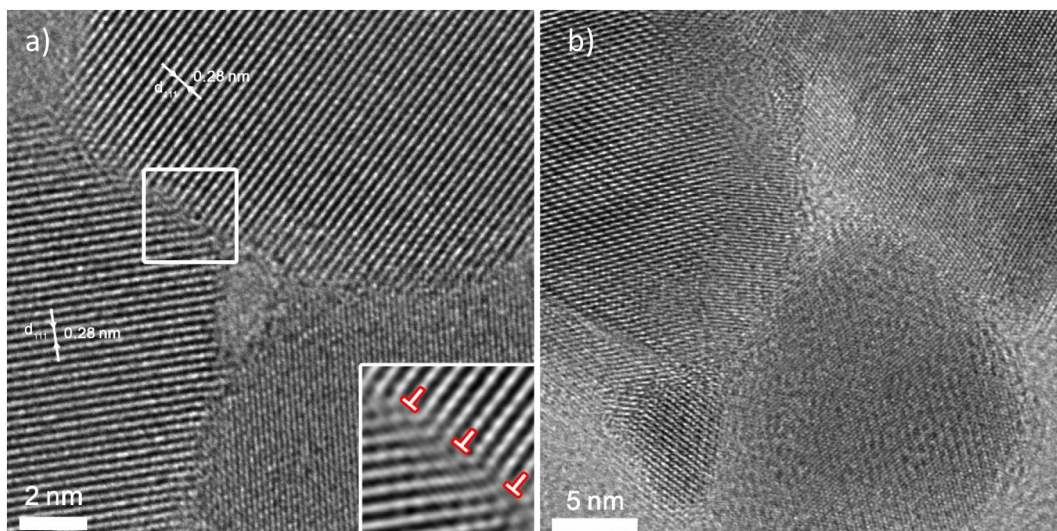


Fig. 4. a) HRTEM micrograph of the sintered sample showing cavity nucleation at grain boundary triple junction and plastic interfaces highlighted by the presence of dislocation networks as shown on the inset (filtered image). b) HRTEM micrograph of grain boundary triple junctions formed by particles of different sizes or with cavity nucleation.

size effect. This apparent contradiction likely underlines the role of constraints and more specifically the contribution of stress gradients arising from both the very high applied external pressure during sintering and the surface strain given the size range of the crystallites (<20 nm) [42]. Competitive and/or combined size and stress effects will be deeply investigated to deciphered the complex stress-size-structure relationships in such nanostructure.

Finally, the combination of a very high density of grain boundaries (grain size lower than 20 nm) with a homogeneous distribution of *meso*/microporosities ensures a cohesive nanostructure that could contribute to explain a hardness as high as 3.8 GPa for a sintering temperature of only 350 °C. Deeper investigations are nevertheless required to evaluate the mobility of grain boundaries and to determine more accurately their impact on the mechanical properties. Our approach based on the use of specific amorphous hydrated precursor to trigger the *in situ* formation of zirconia, and the fast kinetics of SPS, allows yielding, in a single low temperature step, functional zirconia ceramics with a specific nanostructure and whose properties could be of interest in the field of thermal barriers.

Acknowledgements

We thank Eric Lebraud for PXRD measurements and Sébastien Fourcade for TGA and IR analyses. The authors acknowledge PLACAMAT (UMS 3626 CNRS-Bordeaux University) for technical support. This research used resources of the Advanced Photon Source, a U.S. Department of Energy (DOE) Office of Science User Facility operated for the DOE Office of Science by Argonne National Laboratory under Contract No. DE-AC02-06CH1157. The authors thank Dr. Olaf Borkiewicz for assistance with PDF measurements.

Appendix A. Supplementary data

Supplementary data to this article can be found online at <https://doi.org/10.1016/j.scriptamat.2019.04.037>.

References

- [1] D. Sohrabi, B. Heidary, M. Lanagan, C.A. Randall, J. Eur. Ceram. Soc. 38 (2018) 1018–1029.
- [2] J.P. Maria, X.Y. Kang, R.D. Floyd, E.C. Dickey, H.Z. Guo, J. Guo, A. Baker, S. Funihashi, C.A. Randall, J. Mater. Res. 32 (2017) 3205–3218.
- [3] J. Guo, A.L. Baker, H. Guo, M. Lanagan, C.A. Randall, J. Am. Ceram. Soc. 100 (2017) 669–677.
- [4] X. Zhao, J. Guo, K. Wang, T. Herisson De Beauvoir, B. Li, C.A. Randall, Adv. Eng. Mater. 20 (2018) 1700902.
- [5] H. Kähäri, P. Ramachandran, J. Juuti, H. Jantunen, Int. J. Appl. Ceram. Technol. 14 (2017) 50–55.
- [6] S. Grasso, Yoshio Sakka, Giovanni Maizza, Sci. Technol. Adv. Mater. 10 (2009), 053001.
- [7] F. Maglia, I.G. Tredici, U. Anselmi-Tamburini, J. Eur. Ceram. Soc. 33 (2013) 1045–1066.
- [8] R. Chaim, G. Chevallier, A. Weibel, C. Estournès, J. Mater. Sci. 53 (2018) 3087–3105.
- [9] S. Funahashi, J. Guo, H. Guo, K. Wang, A.L. Baker, K. Shiratsuyu, C.A. Randall, J. Am. Ceram. Soc. 100 (2017) 546–553.
- [10] A. Ndayishimiye, A. Largeteau, S. Mornet, M. Duttine, M.-A. Dourges, D. Denux, M. Verdier, M. Gouné, T. Hérisson de Beauvoir, C. Elissalde, G. Goglio, J. Eur. Ceram. Soc. 38 (2018) 1860–1870.
- [11] A. Ndayishimiye, A. Largeteau, M. Prakasam, S. Pechev, M.A. Dourges, G. Goglio, Scr. Mater. 145 (2018) 118–121.
- [12] A. Ndayishimiye, S. Buffière, M.A. Dourges, A. Largeteau, M. Prakasam, S. Mornet, O. Kaman, J. Zdenek, J. Hejtmánek, G.G. Goglio, Scr. Mater. 148 (2018) 15–19.
- [13] G. Goglio, A. Ndayishimiye, A. Largeteau, C. Elissalde, Scr. Mater. 158 (2019) 146–152.
- [14] J. Gonzalez-Julian, K. Neuhaus, M. Bernemann, J. Pereira da Silva, A. Laptev, M. Bram, O. Guillon, Acta Mater. 144 (2018) 116–128.
- [15] J. Nie, Y. Zhang, J.M. Chan, R. Huang, J. Luo, Scr. Mater. 142 (2018) 79–82.
- [16] T. Herisson de Beauvoir, A. Sangregorio, I. Cornu, C. Elissalde, M. Josse, J. Mater. Chem. C 6 (2018) 2229–2233.
- [17] T. Herisson de Beauvoir, F. Molinari, U.C. Chung-Seu, D. Michau, D. Denux, M. Josse, J. Eur. Ceram. Soc. 38 (2018) 3867–3874.
- [18] T. Hérisson de Beauvoir, A. Sangregorio, A. Bertrand, D. Michau, U.C. Chung, M. Josse, Ceram. Int. 45 (2019) 9674–9678.
- [19] H. Guo, J. Guo, A. Baker, C.A. Randall, J. Am. Ceram. Soc. 100 (2017) 491–495.
- [20] R.C. Garvie, R.H. Hannink, R.T. Pascoe, Nature 258 (1975) 703–704.
- [21] X. Ren, W. Pan, Acta Mater. 69 (2014) 397–406.
- [22] C. Piconi, G. Maccauro, Biomaterials 20 (1999) 1–25.
- [23] J. Chevalier, L. Gremillard, A.V. Virkar, D.R. Clarke, J. Am. Ceram. Soc. 92 (2009) 1901–1920.
- [24] J. Kieffer, J.P. Wright, Powder Diffract. 28 (2013) S339–S350.
- [25] P. Juhas, T. Davis, C.L. Farrow, S.J.L. Billinge, J. Appl. Crystallogr. 46 (2013) 560–566.
- [26] T.O.P.A.S. Bruker, V6.0. Bruker AXS, Karlsruhe, Germany, 2015.
- [27] C. Combes, C. Rey, Acta Biomater. 6 (2010) 3362–3378.
- [28] R. Chaim, Nanocrystalline ZrO₂ by crystallization of amorphous oxide, in: M. Nastasi, D.M. Parkin, H. Gleiter (Eds.), Mechanical properties and deformation Behavior of materials having Ultra-Fine Microstructures, NATO ASI Series E: Applied Sciences, 233, 1993, pp. 547–557.
- [29] J. Livage, J. Am. Ceram. Soc. 51 (1968) 349–353.
- [30] R.C. Garvie, J. Phys. Chem. 82 (1978) 218–224.
- [31] S. Tsunekawa, S. Ito, Y. Kawazoe, J.T. Wang, Nano Lett. 3 (2003) 871–875.
- [32] J.R. Soliz, A.D. Klevich, C.R. Harris, J.A. Rossin, A. Ng, R.M. Stroud, A.J. Hauser, G.W. Peterson, J. Phys. Chem. C 120 (2016) 26834–26840.
- [33] B.K. Kim, J.W. Hahn, K.R. Han, J. Mater. Sci. Lett. 16 (1997) 669–671.
- [34] G. King, J.R. Soliz, W.O. Gordon, Inorg. Chem. 57 (2018) 2797–2803.
- [35] A.C. Dippel, K.M.O. Jensen, C. Tyrsted, M. Bremholm, E.D. Bojesen, D. Saha, S. Birgisson, M. Christensen, S.J.L. Billinge, Bo.B. Iversen, Acta Cryst A72 (2016) 645–650.
- [36] V. Petkov, Y. Ren, M.R. Suchomel, J. Phys. Condens. Matter 24 (2012), 155102.
- [37] J.A. Munoz Tabares, M.J. Anglada, J. Am. Ceram. Soc. 93 (2010) 1790–1795.
- [38] J. Luo, R. Stevens, Ceram. Int. 25 (1999) 281–286.
- [39] R. Chintapalli, A. Mestra, F.G. Marro, H. Yan, M. Reece, M. Anglada, Materials 3 (2010) 800–814.
- [40] B. Wojtowicz, W. Pyda, A. Labuz, Ceram. Sliki 57 (2013) 185–189.
- [41] Unpublished work.
- [42] G. Philippot, M. Albino, R. Epherre, G. Chevallier, A. Weibel, A. Peigney, M. Deluca, C. Elissalde, M. Maglione, C. Aymonier, C. Estournès, Adv. Electron. Mater. 1 (2015), 1500190.